Available online at www.sciencedirect.com
SCIENCE DIRECT®
Journal of Computational Physics 209 (2005) 371–389
JOURNAL OF COMPUTATIONAL PHYSICS
www.elsevier.com/locate/jcp

Nonlinear dynamics and loop formation in Kirchhoff rods with implications to the mechanics of DNA and cables

S. Goyal [a], N.C. Perkins [a,*], C.L. Lee [b]

[a] *Mechanical Engineering, 2250 G. G. Brown Laboratories, University of Michigan, 2350 Hayward Street, Ann Arbor, MI 48109-2125, United States*
[b] *Lawrence Livermore National Laboratory, New Technologies Engineering Division, 7000 East Avenue, Livermore, CA 94550, United States*

Received 6 August 2004; received in revised form 2 March 2005; accepted 9 March 2005
Available online 23 May 2005

Abstract

The paper contributes a general dynamical formulation and numerical solution procedure for studying nonlinear and three-dimensional dynamics of Kirchhoff rods. Target applications include the dynamic formation of DNA loops and supercoils as well as loops (hockles) in marine cables. The formulation accommodates non-homogeneous and non-isotropic inextensible rods both with and without coupling of tension and torsion. The utility of this formulation is illustrated by studying the dynamics and quasi-static response of a clamped–clamped rod subject to compression and/or twist. For slow loading rates, the computed quasi-static responses converge to published equilibrium solutions for a benchmark problem. As loading rates increase, new behaviors are observed including hysteresis in the neighborhood of equilibrium bifurcations. The addition of chirality in the form of tension–torsion coupling has a pronounced influence on the computed looped geometries. This finding has implications for DNA loops formed by DNA–protein binding as well as loop formation in helically wound wire and synthetic cables.

Keywords: Kirchhoff rod; Dynamics; Supercoiling; Looping; Cable mechanics; DNA mechanics

1. Introduction

Marine cables under torsion and low tension may form loops and tangles as shown in Fig. 1. In this context, the loops are sometimes referred to as "hockles" and these can lead to mechanical damage or to signal attenuation in fiber optic cables [1]. The resulting large deformations are dominated by bending and torsion

* Corresponding author. Tel.: +1 734 936 0403; fax: +1 734 615 6647.
E-mail address: ncp@umich.edu (N.C. Perkins).

0021-9991/$ - see front matter © 2005 Elsevier Inc. All rights reserved.
doi:10.1016/j.jcp.2005.03.027

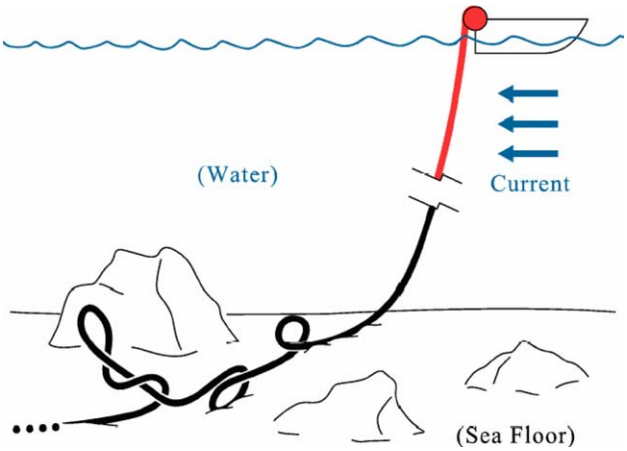

Fig. 1. Low tension cable forming loops and tangles on the sea floor.

as captured in elastic rod theories; refer, for example, to [1–4]. Loop formation in elastic rods is often initiated by instabilities under compression and/or torsion.

Rod theories are commonly used to understand the mechanics of long structural elements such as marine and satellite tethers and cables. At small length scales, the same rod theories have been employed to model biological filaments and single molecules including cilia, flagella, and DNA; see for example [5–7]. Despite enormous differences in these length scales and applications, some striking similarities exist. For instance, interwound DNA supercoils are topologically equivalent to the hockles that may form in marine cables [8]. In addition, the helical construction of synthetic and wire rope cables produces a chiral structure that resembles that of the DNA duplex. Averaged over many helical turns, the bending and torsional stiffness of cables and DNA influence their response to applied forces which, in turn, may greatly impact their function/performance. For instance, the structural behavior of DNA influences its functional behavior including gene expression [9–12]. The structural response of DNA, and the formation of loops and supercoils, requires multi-physical modeling that may include, for example, structural stiffness, hydrodynamics, electrostatics, and thermal kinetics [6,13].

Classical Kirchhoff/Clebsch rod theory employs a linear elastic constitutive law for bending and torsion, and large deformations produce geometric nonlinearities in the resulting equilibrium equations [14–17]. Numerous studies have employed this nonlinear static rod theory to compute looped geometries representing three-dimensional *equilibrium* states; see for example [2,3,18,19]. Recent studies have also accounted for self-contact in looped equilibrium states [20,21]. It is well known that both planar and non-planar equilibrium states may become unstable under specific bifurcation conditions; consider, for instance, the loop formation instabilities noted in [2,21] and the opposite "pop-out" instabilities noted in [3,21]. These instabilities initiate large *dynamic* responses which may also produce nonlinear transitions to more energetically favorable equilibria. Few studies, however, have investigated nonlinear dynamic responses.

The model in [5] is used to study quasi-static response with self-contact, while that in [22,23] captures highly dynamic responses damped by hydrodynamic forces but without self-contact. The latter model is extended in [8] for non-homogeneous and anisotropic rods and again in [24] for dynamic self-contact. The dynamic evolution of a hockle (or equivalently an interwound DNA supercoil) with self-contact is simulated in [24]. Anisotropy in the *equilibrium* rod models for DNA has been evaluated in [25,26].

The first objective of the present study is to benchmark results from the dynamic rod model [8] with the predicted equilibrium states and bifurcation conditions recently presented in [21]. This benchmark

problem considers clamped rods subject to twist and compression. Two further objectives are to understand the influence of (1) nonlinear rod dynamics, and (2) the coupling of tension and torsion in chiral rods.

We open in Section 2 by presenting the dynamical rod theory as a 12th-order initial-boundary value problem. An efficient finite difference solution method is then reviewed in Section 3 that employs the generalized-α method [27–29] in both space and time. Nonlinear kinematics of rod rotation are formulated using incremental rotations [30] as opposed to previous Euler parameter formulations [31]. The benchmark problem is evaluated in Section 4 and comparisons are drawn between the dynamical solutions captured herein with the equilibrium solutions of [21]. The dynamical solutions converge to the equilibrium solutions under quasi-static loading. They also exhibit a variety of nonlinear dynamic transitions between equilibria and hysteresis as the loading rates increase. Examples of hysteresis are included in Section 5. In Section 6, we study the influence of chirality by adding tension–torsion coupling to the rod constitutive law. This coupling is motivated by the helically wound construction of common wire and synthetic cables as well as the DNA duplex. The impact of this coupling is highlighted through new solutions to the benchmark problem. We close with conclusions in Section 7.

2. Dynamical rod model

2.1. Definitions and assumptions

Consider the infinitesimal element of a Kirchhoff rod [14] with the deformation field determined by the centerline curvature and cross-section twist. The body-fixed frame $\{a_i\}$ at each cross-section is employed to describe the orientation of the cross-section with respect to the inertial frame $\{e_i\}$. The three-dimensional curve formed by the centerline is parameterized by the arc length coordinate s and time t. The deformation field is represented by the curvature and twist vector $\kappa(s,t)$ that is defined as the rotation per unit arc length of the body-fixed frame. In a stress-free state, the rod conforms to its natural geometry (with possible intrinsic curvature and twist) defined by $\kappa_0(s)$.

The internal stress resultants generate tension (or compression), shear, and bending and torsional moments on the cross-section. The resultant internal force and internal moment vectors are denoted by $f(s,t)$ and $q(s,t)$, respectively. The Kirchhoff rod is unshearable and inextensible, and employs a linear elastic constitutive law relating the internal moments to the curvature and twist

$$q(s,t) = B(s)(\kappa(s,t) - \kappa_0(s)), \tag{1}$$

where $B(s)$ is a (positive definite) stiffness tensor. The resulting strain energy per unit arc length becomes

$$S_e(s,t) = \frac{1}{2}(\kappa(s,t) - \kappa_0(s))^T B(s)(\kappa(s,t) - \kappa_0(s)). \tag{2}$$

The kinetic energy of the rod depends upon the centerline velocity $v(s,t)$ and the cross-section angular velocity $\omega(s,t)$. Let $m(s)$ denote the mass of the rod per unit arc length and $I(s)$ denote the tensor of principal mass moments of inertia per unit arc length. Then the kinetic energy per unit arc length is

$$K_e(s,t) = \frac{1}{2}\omega(s,t)^T I(s)\omega(s,t) + \frac{1}{2}v(s,t)^T m(s)v(s,t). \tag{3}$$

The vectors $v(s,t)$, $\omega(s,t)$, $\kappa(s,t)$, and $f(s,t)$ define four field variables. Depending upon the application, the rod may also interact with numerous external field forces including those produced by gravity, a surrounding fluid medium, contact with other bodies or with the rod itself, electrostatic forces, Langevin (thermal) forces, etc. An overview of example hydrodynamic and thermal forces is provided in Appendix 1. The

resultant of these external forces and moments per unit length is denoted by $F(s,t,\ldots)$ and $Q(s,t,\ldots)$, respectively, and these may also depend upon the kinematical quantities $\kappa(s,t)$, $\omega(s,t)$, and $v(s,t)$.

Unless stated otherwise, the vector quantities will be represented using components in the body fixed frame $\{a_i\}$. Recall that partial derivatives of any vector v with respect to the body fixed frame are related to the partial derivatives with respect to the inertial frame through

$$\left(\frac{\partial v}{\partial t}\right)_{\{a_i\}} = \left(\frac{\partial v}{\partial t}\right)_{\{e_i\}} - \omega \times v \quad \text{and} \quad \left(\frac{\partial v}{\partial s}\right)_{\{a_i\}} = \left(\frac{\partial v}{\partial s}\right)_{\{e_i\}} - \kappa \times v, \tag{4}$$

where the subscript specifies the reference frame. For notational convenience, we drop the subscript for the body fixed frame from this point forward.

The body fixed frame $\{a_i\}$ is chosen to coincide with the 'principal torsion-flexure axes' of the cross-section [16]. In particular, a_1 and a_2 are in the plane of the cross-section and are aligned with the principal flexure axes while a_3 is normal to the cross-section (directed towards increasing arc length) and coincides with the torsion axis. Expressed in this reference frame, the tensors $B(s)$ and $I(s)$ are diagonal. For example, $B(s)$ reduces to

$$B(s) = \begin{bmatrix} A_1(s) & 0 & 0 \\ 0 & A_2(s) & 0 \\ 0 & 0 & C(s) \end{bmatrix}, \tag{5}$$

where $A_1(s)$ and $A_2(s)$ are bending rigidities (possibly non-homogeneous and/or non-anisotropic), and $C(s)$ is the torsional rigidity.

2.2. Equations of motion

The balance of linear momentum of the infinitesimal element shown in Fig. 2 becomes

$$\frac{\partial f}{\partial s} + \kappa \times f = m\left(\frac{\partial v}{\partial t} + \omega \times v\right) - F \tag{6}$$

and the balance of angular momentum becomes

$$\frac{\partial q}{\partial s} + \kappa \times q = I\frac{\partial \omega}{\partial t} + \omega \times I\omega + f \times a_3 - Q. \tag{7}$$

Recall that the internal moment q is related to the curvature and twist κ through the constitutive law (1).

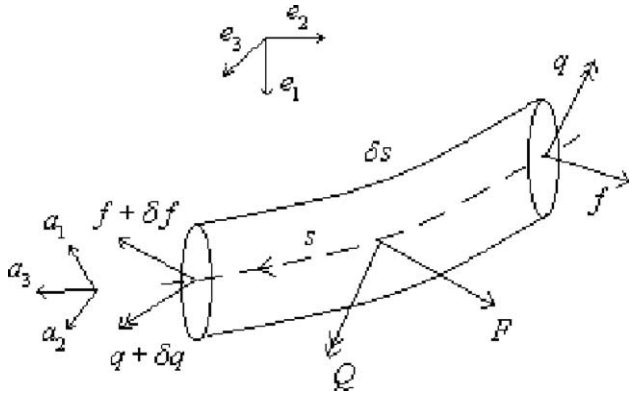

Fig. 2. Free body diagram of an infinitesimal element of a Kirchhoff rod.

2.3. Constraints and summary

The above formulation is completed with the addition of two constraints. The first enforces an inextensibility constraint which takes the form

$$\frac{\partial v}{\partial s} + \kappa \times v = \omega \times a_3. \tag{8}$$

The second follows from continuity requirements for ω and κ in the form of the compatibility constraint

$$\frac{\partial \omega}{\partial s} + \kappa \times \omega = \frac{\partial \kappa}{\partial t}. \tag{9}$$

Derivations of these constraints are provided in Appendix 2.

The four vector equations (6)–(9) in the four vector unknowns $\{v, \omega, \kappa, f\}$ are compactly written as

$$M(Y,s,t)\frac{\partial Y}{\partial t} + K(Y,s,t)\frac{\partial Y}{\partial s} + \mathbb{F}(Y,s,t) = 0, \tag{10}$$

where $Y(s,t) = \{v, \omega, \kappa, f\}$. The matrices M, K and $\mathbb{F}$ are defined in Appendix 3.

3. Numerical algorithm

Eq. (10) is 12th-order in space and requires six boundary conditions at the two boundary points. The generalized-α method [27–29] is employed for integration in both space and time, leading to a second-order accurate implicit finite differencing algorithm. The method is unconditionally stable and has the advantage of controllable numerical dissipation. Starting with the initial value $Y(s,0)$, the discretized equations are integrated over space at each successive time step. The boundary conditions are satisfied during spatial integration using classical shooting for boundary-value problems [23].

The boundary conditions and distributed forces/moments are often most readily decomposed into components in the inertial frame. During integration, these components must be transformed to those in the body fixed frame through a transformation matrix $L(s,t)$. Standard formulations employ three Euler angles or four Euler parameters to construct the nine components of $L(s,t)$. Here, we employ incremental rotations [30]. Accordingly, we compute the small change in $L(s,t)$ across the time step Δt using the small incremental rotation $\Phi(s,t,t-\Delta t)$

$$L(s,t) = \Phi(s,t,t-\Delta t)L(s,t-\Delta t). \tag{11}$$

This rotation can be accomplished through a single rotation about one axis by invoking the Euler rotation theorem [31]. Let the vector $\theta(s,t)$ represent the infinitesimal rotation vector for $\Phi(s,t,t-\Delta t)$. Then

$$\omega(s,t) = \lim_{\Delta t \to 0} \frac{\theta(s,t)}{\Delta t} \quad \text{and} \quad \Phi = \exp(-\tilde{\theta}), \tag{12}$$

where $\tilde{\theta}$ is the skew-symmetric form of θ defined in Appendix 4. In short, we use (12) to compute $\theta(s,t)$ and $\Phi(s,t)$ and then use (11) to update $L(s,t)$. From the transformation matrix $L(s,t)$ and the centerline velocity $v(s,t)$, we then compute the position and orientation of each cross-section of the rod at any time by subsequent integration.

4. Benchmarking study

We begin by comparing results from the dynamic model above with published equilibrium solutions that serve as benchmarks. One benchmark study [21] catalogs the equilibria and bifurcations of homogeneous isotropic rods ($A_1(s) = A_2(s) = A$) subject to specified end twist and end separation as illustrated in Fig. 3. These equilibrium solutions are recovered as quasi-static solutions in our formulation for slow loading rates. In [21], the rod is further assumed to have no distributed forces or moments and no intrinsic curvature or twist. The bending to torsional stiffness ratio is chosen as $A/C = 1.4$. We include drag [23] as the means to incorporate dissipation and also as a means to introduce a small random disturbance through a small random superimposed flow.

4.1. Initial and boundary conditions

The rod of Fig. 3 has a specified number of complete twists $\mathbb{R}$ when straight. This number of twists is also referred to as the "end rotation" in [21]. This equilibrium configuration is chosen as the initial condition for all subsequent simulations. Both ends are then clamped. One clamp is then moved towards the other through a distance $d(t)$ normalized by the rod arc length L_c. The quantity d is referred to as the "end shortening" in [21], and it increases from $d = 0$ for the initially straight rod, through $d = 1$ when the two ends meet, to the limit $d \to 2$ when the two ends cross and the rod is pulled straight (with infinite curvature at the boundaries). In the absence of self-contact, the clamped ends may pass by each other during this process. A formulation that incorporates dynamic self-contact is the subject of [24].

At slow (quasi-static) loading rates, $\dot{d} \to 0$ and our solutions converge to steady-state solutions. Table 1 lists the loading rate along with the other parameters that were used to obtain the following results. We compute the end tension (referred to as the "rig force" in [21]) using

$$P(t) = \frac{f_3(0,t)L_c^2}{4\pi^2 A} \tag{13}$$

which is normalized by the fundamental Euler buckling load. As the ends slowly approach, the rod initially buckles in its fundamental buckling mode as expected. The end tension and torque required to initiate buckling (of a twisted clamped rod) is derived in [32] as the buckling condition

$$\cos\left(\pi\sqrt{T^2 - 4P}\right) - \cos(\pi T) = \frac{2\pi P \sin\left(\pi\sqrt{T^2 - 4P}\right)}{\sqrt{T^2 - 4P}}. \tag{14}$$

Here, T is the (normalized) end torque that is referred to as the "rig moment" in [21]

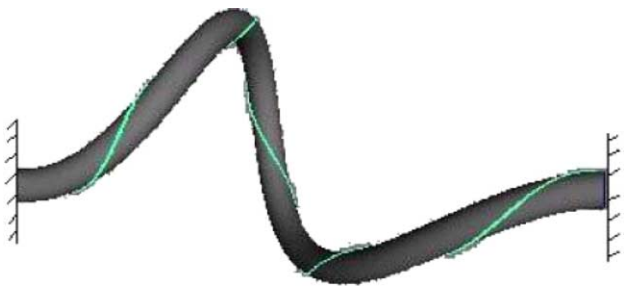

Fig. 3. Benchmark problem: a twisted and clamped rod. The ends have prescribed twist and separation.

Table 1
Rod and simulation parameters

Quantity	Units (SI)	Value
Rod diameter D	m	1.0×10^{-3}
Rod length L_c	m	1.0×10^{0}
Bending stiffness A	N m^2	$\frac{1.4\pi}{64}\times10^{-3}$
Torsional stiffness C	N m^2	$\frac{\pi}{64}\times10^{-3}$
Bending moments of inertia per unit length I_1 and I_2	kg m	$\frac{\pi}{64}\times10^{-9}$
Torsional moment of inertia per unit length I_3	kg m	$\frac{\pi}{32}\times10^{-9}$
Fluid density ρ_f	kg/m^3	1.0×10^{0}
Normal drag coefficient C_n	–	1.0×10^{-1}
Tangential drag coefficient C_t	–	1.0×10^{-2}
Quasi-static loading rate $\lvert\dot{d}\rvert$ (Section 4)	m/s	5.0×10^{-3}
Non-equilibrium loading rate $\lvert\dot{d}\rvert$ (Section 5)	m/s	5.0×10^{-2}
Temporal step Δt	s	1.0×10^{-1}
Spatial step Δs	m	1.0×10^{-2}

$$T(t)=\frac{q_3(0,t)L_c}{2\pi A}. \tag{15}$$

4.2. Case 1: $\mathbb{R}=0$, planar buckling at quasi-static rates ($\dot{d}\to 0$)

We begin with the simplest case of a straight rod with no initial twist ($\mathbb{R}=0$) and evaluate its response to quasi-static compression as the end shortening increases at a very slow rate ($\dot{d}\to 0$). To initiate and to maintain buckling in one plane, we add a very small random fluid flow in the plane which loads the rod through hydrodynamic drag as detailed in Appendix 5. The computed end tension is plotted in Fig. 4(a) as a function of the end shortening d for the dynamic formulation presented herein (blue curve). This dynamic solution converges to the equilibrium solutions reported in [21] (red curves) for this quasi-static loading rate ($\dot{d}\to 0$). The curves labeled 1 and 2 designate equilibrium solutions for the first and second buckling modes, respectively. Starting at $d=0$, the dynamic solution follows the equilibrium solution for

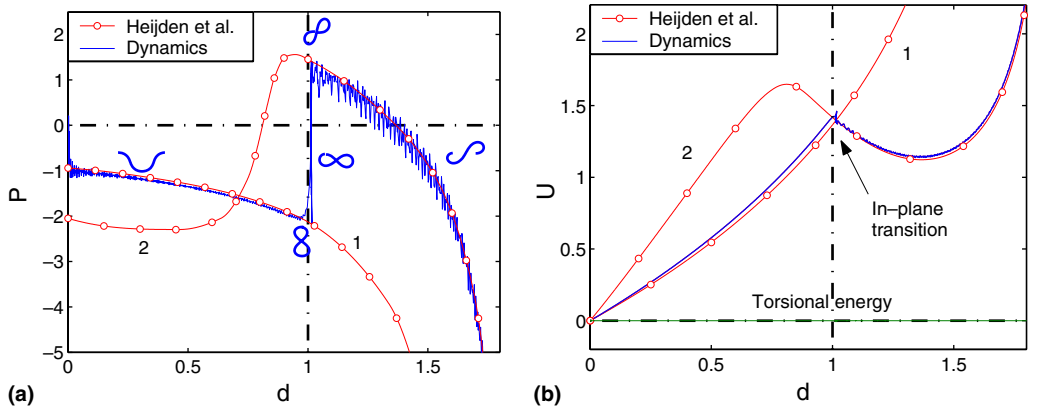

Fig. 4. Planar buckling at quasi-static rates ($\mathbb{R}=0,\ \dot{d}\to 0$). The end tension (a) P and the strain energy (b) U are plotted as functions of the end shortening d. The (red) curves labeled 1 and 2 replicate solutions from [21] for the first and second buckling modes, respectively. The (blue) curve represents the (quasi-static) solution from the dynamic model. (For interpretation of the references to color in this figure legend, the reader is referred to the web version of this article.)

the fundamental mode and at $d = 1$ undergoes a large *dynamic* transition to the solution for the second mode. This transition results as the second mode becomes more energetically favorable (lower strain energy) for $d > 1$.

This fact is illustrated in Fig. 4(b) where the strain energy is plotted as a function of end shortening. For these planar equilibria, the strain energy develops solely from bending (no torsion) as computed from the strain energy density (2):

$$U(t) = \frac{L_c}{4\pi^2 A} \int_0^{L_c} S_e(s,t)\, ds. \tag{16}$$

The strain energy for the equilibrium solutions (red curves) is computed from the work done at the boundary using the known end tension [21] and by noting

$$P = -\frac{\partial U}{\partial d}. \tag{17}$$

The dynamic solution tracks the strain energy for the fundamental buckling mode for $d < 1$ and then for the second buckling mode for $d > 1$. During this transition, the rod forms the sequence of figure eight configurations shown in Fig. 5 as computed by the dynamic formulation herein. This transition converges to that reported in [33] for the quasi-static loading considered in this example. Note that the clamped ends start at the apex of figure eight (snapshot 2) and ultimately transition to the intersection of figure eight (snapshot 4). The same transition is reproduced upon decreasing d and without the hysteresis observed at faster loading rates as discussed in Section 5.

4.3. Case 2: $\mathbb{R} = 0$, Spatial buckling at quasi-static rates ($\dot{d} \to 0$)

We now re-evaluate the above example upon the addition of a small three-dimensional random disturbance that initiates an out-of-plane instability; refer to Appendix 5. In particular, the planar equilibria now become unstable beyond a critical end shortening and bifurcate into stable spatial (three-dimensional) equilibria [21]. The end tension computed in [21] is recovered for the quasi-static loading rates in this example as reported in Fig. 6(a) (red curve). The rod now buckles out of plane (follow blue curve) well before reaching a figure eight configuration. This bifurcation is denoted by the triangle in Fig. 6 which locates where the fundamental in plane mode loses stability and a stable spatial buckling mode is born. In addition, the rod deforms into a circular loop with one complete twist at $d = 1$ as bending strain energy (red curve) is exchanged for torsional strain energy (green curve) in Fig. 6(b). In fact, there is a marked decrease in bending energy accompanied by a large increase in torsional energy just beyond the bifurcation point which initiates the out of plane deformation.

4.4. Case 3: $|\mathbb{R}| = 1$ Planar and spatial buckling at quasi-static rates ($\dot{d} \to 0$)

The calculations above are now repeated after first pre-twisting the rod by introducing one complete end rotation when the rod is straight, i.e., $|\mathbb{R}| = 1$. The end tension for both planar and spatial equilibria [21] is

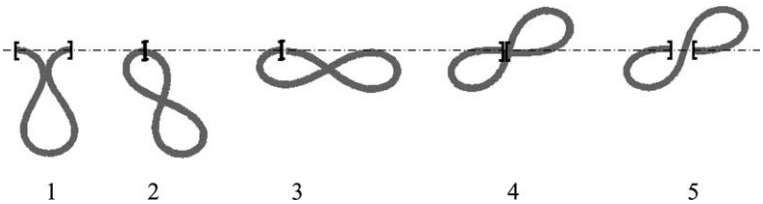

Fig. 5. Dynamic transition from first buckling mode (snapshot 1) to second buckling mode (snapshot 5) through a series of figure eight configurations. The non-equilibrium shapes (snapshots 2–4) correspond to the dynamic transition path in Fig. 4(a).

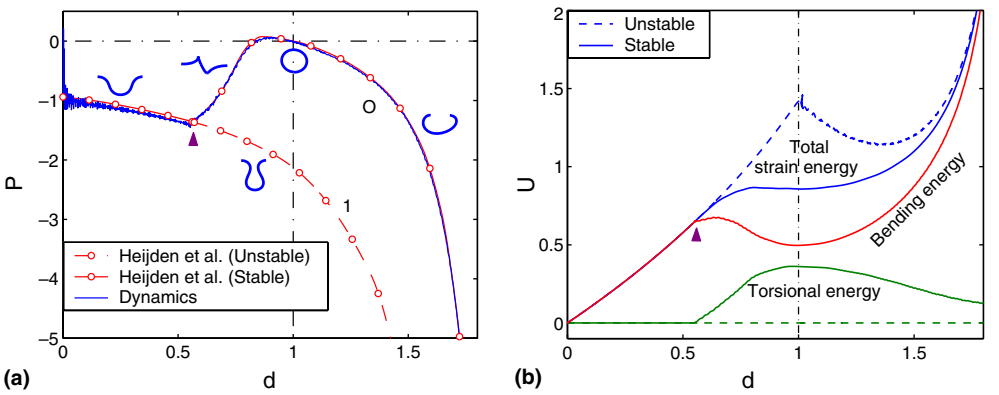

Fig. 6. Spatial buckling at quasi-static rates ($\mathbb{R} = 0,\ \dot{d} \to 0$). The end tension (a) P and the strain energy (b) U are plotted as functions of the end shortening d. The (red) curves labeled 1 and O replicate equilibrium solutions from [21] and the solid (dashed) curve represents stable (unstable) equilibria. The out of plane bifurcation point is denoted by the triangle. The strain energy (blue) is the sum of torsional (green) and bending (red) strain energies. (For interpretation of the references to colour in this figure legend, the reader is referred to the web version of this article.)

recovered for the quasi-static loading rate used in this example; refer to Fig. 7(a). Starting from $d = 0$, the rod first buckles as per (14) in its fundamental mode which resembles a helix with small helical diameter [32]. The helical diameter increases with d and the spatial equilibrium ultimately becomes planar with an interior loop at the bifurcation point (denoted by the triangle). At this bifurcation, the out of plane solution branch denoted by O joins the fundamental in plane solution branch denoted by 1. As d is increased further, the now planar loop increases in diameter, and at $d = 1$, the rod conforms to a circular loop (without twist). This loop becomes flattened for $d > 1$ and remains planar as it approaches the limit $d \to 2$ at which point the rod is again straight with infinite curvature at its extremities. If the process is reversed (i.e., d is now slowly decreased from 2), the planar loop becomes unstable at the bifurcation and exhibits a "pop out"

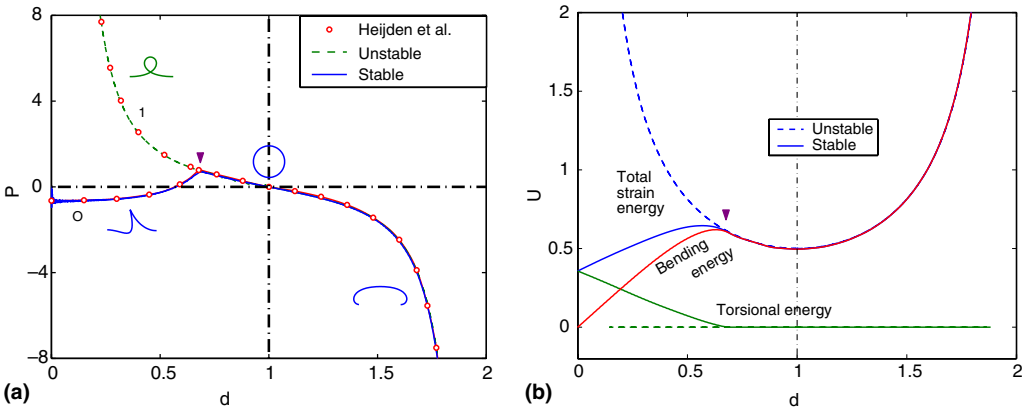

Fig. 7. Effect of initial twist on the spatial and planar buckling at quasi-static rates ($\mathbb{R} = 1,\ \dot{d} \to 0$). The end tension (a) P and the strain energy (b) U are plotted as functions of the end shortening d. The curves labeled 1 and O replicate equilibrium solutions from [21] and the solid (dashed) curve represents stable (unstable) equilibria. The bifurcation point is denoted by the triangle. The strain energy U (blue) is the sum of torsional (green) and bending (red) strain energies. (For interpretation of the references to colour in this figure legend, the reader is referred to the web version of this article.)

instability [3] when subjected to minute three-dimensional excitation. Fig. 7(b) shows that the strain energy (and its decomposition into torsional and bending components) for the solutions of Fig. 7(a). Starting with the straight and twisted rod ($d = 0$), the strain energy develops purely from torsion. Upon buckling, the torsional strain energy is reduced while the bending strain energy is increased and a net increase in strain energy results as the spatial equilibria evolve (d increases). At the bifurcation point, the strain energy of the spatial equilibrium achieves that of the planar equilibrium and beyond that point only the planar solution exists.

It should also be noted in Fig. 7(b) that the circular loop ($d = 1$) achieves the minimum strain energy beyond the bifurcation point. This coincides with the fact all circular loops with twist less than a critical value ($|\mathbb{R}| < \sqrt{3}\frac{A}{C}$) are stable [4,21,34,35]. Above this critical value, the circular loop buckles into a figure eight (with subsequent intertwining) [5].

5. Effect of non-equilibrium loading (finite $\dot{d}$)

The results above confirm that the dynamic solutions converge to known equilibrium solutions at infinitesimal loading rates $\dot{d} \to 0$. The dynamic formulation reproduces the expected equilibrium bifurcations and dynamic transitions between equilibria are also captured. We now turn attention to cases where the loading rate is finite which introduces new dynamic effects, most notably hysteresis. In particular, as the loading rate increases, the dynamic transition from planar to spatial equilibrium forms is delayed due to inertial effects.

Figs. 8(a) and (b) illustrate this phenomenon for cases of an initially untwisted rod ($\mathbb{R} = 0$) and a rod with one complete initial twist ($|\mathbb{R}| = 1$), respectively. The loading rate $|\dot{d}| = 5 \times 10^{-2}$ m/s is sufficiently large to observe hysteresis in these examples. The remaining parameters used in this example are again listed in Table 1. As above, we include minute random excitation produced by a random flow field as described in Appendix 5.

For the initially untwisted rod, the dynamic solution closely tracks the planar equilibrium solutions as the end shortening initially increases ($\dot{d} > 0$) starting from $d = 0$; refer to black curve in Fig. 8(a). However, near the equilibrium bifurcation point (triangle), the dynamic solutions experience a delayed jump (“pop

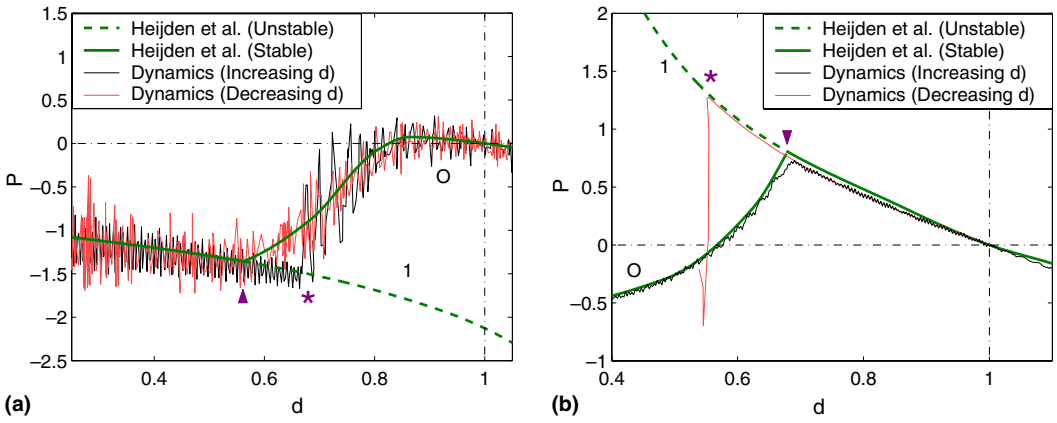

Fig. 8. Dynamic effects of non-equilibrium loading rates ($\dot{d}$ finite). The end tension P plotted as function of end shortening d for cases of rod (a) without initial twist $\mathbb{R} = 0$, and (b) with one complete initial twist $\mathbb{R} = 1$. The curves labeled 1 and O replicate planar and spatial equilibrium solutions from [21]. The equilibrium bifurcation point is denoted by the triangle and the delayed transition by the asterisk. (For interpretation of the references to colour in this figure legend, the reader is referred to the web version of this article.)

out'' instability) from the planar forms to the spatial forms as indicated by the asterisk. By contrast, when the loading rate is reversed ($\dot{d} < 0$), the dynamic solutions pass through the equilibrium bifurcation as the spatial forms transition smoothly to the planar forms; refer to light gray (or red) curve.

Fig. 8(b) shows analogous results for the case of the pre-twisted rod previously evaluated in Fig. 7. As the end shortening increases ($\dot{d} > 0$), the dynamic solution closely follows the spatial form and smoothly transitions to the planar form by passing through the equilibrium bifurcation (triangle); refer to black curve. Upon reversing the loading rate ($\dot{d} < 0$), the dynamic solution experiences a significant delayed jump (''pop out'' instability) from the planar to the spatial forms as indicated by the asterisk; refer to light gray (or red) curve. Increasing the loading rate increases the delay while increasing the random excitation decreases the delay, as expected.

6. Effect of tension–torsion coupling

The benchmark equilibrium problem and the dynamic extensions above employ the constitutive model (1) that also assumes no coupling of torsion and tension. Thus, under pure compression, the rod initially buckles into a planar form and no torsional strain energy develops. By contrast, the initial buckling of rod-like elements may be decidedly three-dimensional due to inherent chirality [36]; consider, for instance, the helically wound structure of wire or synthetic cable [37] or the helical duplex of DNA [38]. In such systems, any tension/compression immediately induces torsion. For marine cable applications, this motivates the need to design so-called ''torque-balanced'' cables by using constructions that incorporate both left-handed and right-handed helical winds. For DNA, this coupling affects the geometry and energetics of protein-mediated DNA loops that are a known regulatory mechanism for gene expression [39–41]. We now add tension–torsion coupling to the rod model above and study its influence on the dynamics of a clamped–clamped rod.

Following [37], we begin with a homogenized linear constitutive law for coupled torsion and extension

$$f_3 = C_1\varepsilon + C_2\kappa_3, \quad q_3 = C_3\varepsilon + C_4\kappa_3. \tag{18}$$

In the context of the wire rope considered in [37], ε denotes the overall extensional strain of the rope (not the individual component wires) and the constants C_i are determined by the stiffness of the component wires and the helical construction. The simple model above captures the observed fact that the component wires tend to unwind as the rope is stretched. Eliminating ε leads to the (linear) tension–torque relation

$$q_3 = C(\kappa_3 - C_5 f_3), \tag{19}$$

where C and C_5 again depend upon the helical construction and wire stiffness. The coupling factor C_5 is non-dimensionalized and renamed k_c using

$$\left(\frac{C_5 f_3 L_c}{2\pi}\right) = k_c\left(\frac{f_3 L_c^2}{4\pi^2 A}\right) \tag{20}$$

for homogeneous and hemitropic rods [36]. We note that the sign of k_c distinguishes a right-handed ($k_c < 0$) helical construction from a left-handed ($k_c > 0$) helical construction. The clamped rod under pure compression ($\mathbb{R} = 0$) will now immediately develop a reaction end torque $T = -k_c\frac{C}{A}P$. Using this result in the buckling condition (14) yields the critical end tension required to initiate buckling for a chiral rod

$$\cos\left(\pi\sqrt{\left(k_c\frac{C}{A}P\right)^2 - 4P}\right) - \cos\left(\pi k_c\frac{C}{A}P\right) = \frac{2\pi P\sin\left(\pi\sqrt{\left(k_c\frac{C}{A}P\right)^2 - 4P}\right)}{\sqrt{\left(k_c\frac{C}{A}P\right)^2 - 4P}}. \tag{21}$$

Fig. 9 shows how this critical end tension depends upon the coupling factor k_c for the first three buckling modes. Clearly, this coupling factor has a strong influence on this bifurcation condition.

Even seemingly weak coupling has a marked influence on the shape of the rod after buckling. This sensitivity is of keen interest in DNA mechanics where long-length scale looping can regulate gene expression [39–41]. The orientation, twist distribution, and curvature distribution along the loop affect the availability of DNA binding sites to transcriptional proteins [25,42]. The overall loop strain energy contributes to the free energy of the DNA/protein complex and thus influences the probability of loop formation. Motivated by these issues, we will now explore how loop properties are influenced by the coupling factor k_c for the simplest case of $\mathbb{R} = 0$.

Fig. 10(a) shows snapshots of the loops formed both with and without tension–torque coupling for one value of end shortening $d = 0.5$ which corresponds to a state slightly before the bifurcation noted in Fig. 6 (triangle). As the coupling factor is increased, the loop rotates significantly out of plane. To quantify this out of plane rotation, we introduce the angle ϕ between the centerline tangent a_3 at the *tip* of the loop and the axis formed by the two ends (coincident with $a_3(0,t)$). We define the *tip* of the loop as the point farthest from the axis formed by the two ends as measured by the distance $|a_3(0,t) \times (R(s,t) - R(0,t))|$. At equilibrium, the loop will exhibit symmetry such that the tip is at the mid-span. In general, we compute the out of plane rotation at the tip using

$$\phi = \cos^{-1}\left(a_3(0,t) \cdot a_3(S_{\text{tip}},t)\right). \tag{22}$$

Fig. 10(b) shows the variation of ϕ as a function of end shortening d for three values of the coupling factor k_c. For cases $k_c \neq 0$, the out of plane rotation is initiated immediately and increases rapidly with increasing end shortening, thus underscoring the sensitivity to tension–torsion coupling.

Fig. 11 shows the spatial variation of the (normalized) torsional moment q_3, tension f_3, twist κ_3, and principal curvature $|\kappa_0 \times a_3|$ for the rods with and without tension–torsion coupling. In this example, the end shortening $d = 0.5$ for the two cases $k_c = 0$ and $k_c = 0.1$. The computed results for the torsional moment q_3 confirm that this quantity remains constant (a first integral) under equilibrium conditions and this constant is also non-zero when tension–torsion coupling exists. This small degree of tension–torsion coupling has only a minor influence on the computed tension f_3 and the principal curvature $|\kappa_0 \times a_3|$, yet a pro-

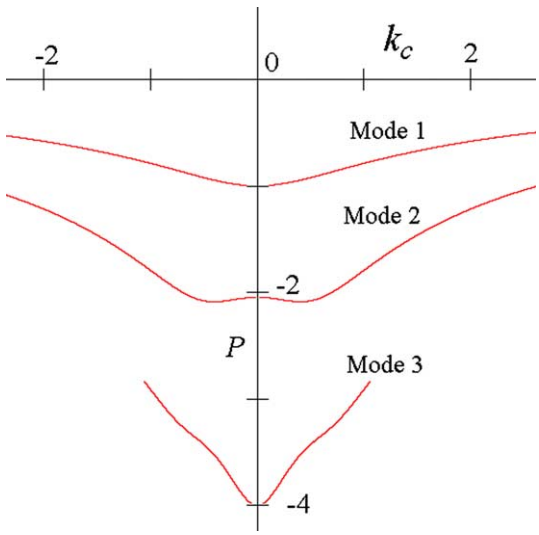

Fig. 9. The critical end tension P that initiates buckling as a function of the coupling factor k_c. Values for the first three modes are computed per (21) with $\mathbb{R} = 0$.

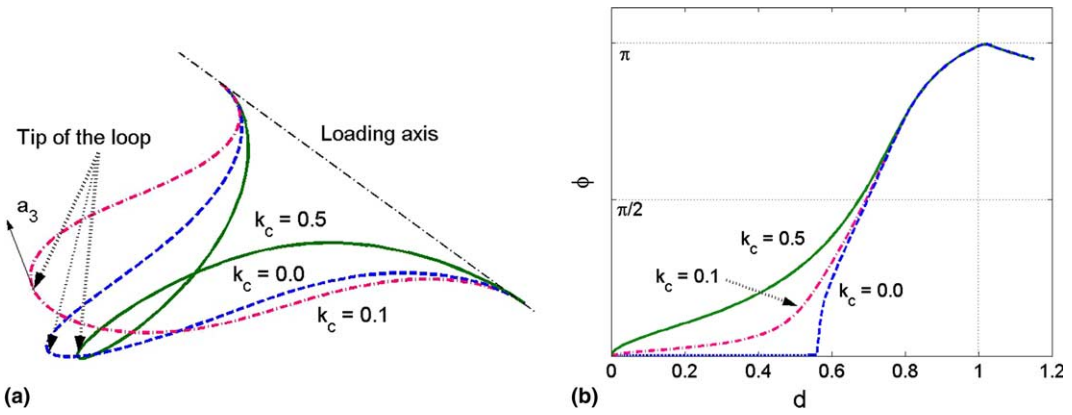

Fig. 10. (a) Sensitivity of equilibrium loop orientations to tension–torsion coupling k_c. End shortening $d = 0.5$ and initial twist $\mathbb{R} = 0$. (b) The angle ϕ, which measures the out of plane orientation of the loop, is plotted as a function of end shortening d for three values of the coupling factor k_c.

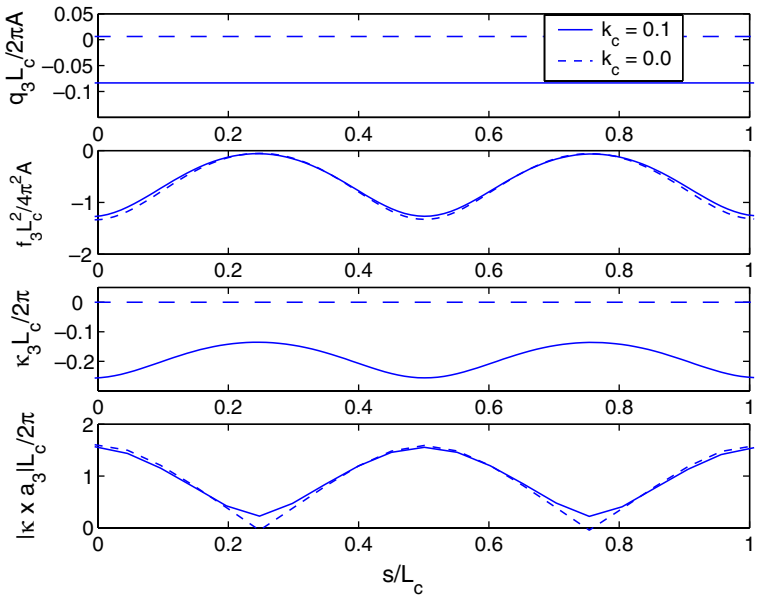

Fig. 11. Distribution of (non-dimensional) torsional moment q_3, tension f_3, twist κ_3 and principal curvature $|\kappa_0 \times a_3|$ with arc length s. End shorting $d = 0.5$ and twist $R = 0$.

nounced influence on the computed twist κ_3. The large influence on twist is responsible for the large sensitivity of loop geometry on tension–torsion coupling as observed above.

7. Conclusions

The paper contributes a general dynamical formulation and numerical solution procedure for studying nonlinear and three-dimensional dynamics of Kirchhoff rods. The model accommodates non-homogeneous

and non-isotropic inextensible rods both with and without coupling of tension and torsion due to chirality. Added drag allows simulation either with or without physical dissipation, while the use of the generalized-α method accommodates (controlled) numerical dissipation. The utility of this formulation is demonstrated by studying the dynamics and quasi-static response of a clamped–clamped rod subject to compression and/or twist.

The quasi-static response is used to benchmark the dynamical formulation with known equilibrium solutions. In particular, the equilibria and bifurcations studied in [21] are replicated over a wide range of quasi-static loading conditions leading to both planar and spatial loops. The inclusion of dynamics makes it possible to study nonlinear transitions between equilibria and to capture the effects of hysteresis. Such transitions may help explain how small thermal fluctuations in DNA can initiate large changes in supercoiled states [40]. The benchmark problem is further extended to accommodate chirality in the form of tension–torsion coupling as found in helically wound wire and synthetic cables and the DNA duplex. Results indicate that, in general, non-planar equilibria form immediately with any end shortening and that the ultimate shape of the loop is a strong function of the tension–torsion coupling. This finding suggests that loop formation (hockling) in wire and synthetic cables will be sensitive to cable construction. In addition, this finding has implications for the possible shapes of protein-mediated DNA loops that are a known regulatory mechanism for gene expression.

Acknowledgments

The authors gratefully acknowledge the research support provided by the US Office of Naval Research, Lawrence Livermore National Laboratories, and the National Science Foundation. The work of Christopher L. Lee was performed under the auspices of the US Department of Energy by the University of California, Lawrence Livermore National Laboratory under Contract No. W-7405-ENG-48. We are also grateful for the many engaging discussions of DNA mechanics and supercoiling with Prof. C. Meiners and S. Blumberg in the Biophysics Program at the University of Michigan.

Appendix 1. Example hydrodynamic and thermal forces

The computational rod model herein incorporates a general body force that may represent a wide range of possible interactions. The interactions appropriate for marine cables are, of course, quite distinct from those governing the mechanics of DNA strands. In particular, the hydrodynamic and thermal forces are significantly different for these two applications and example (not exhaustive) formulations of each are included in this appendix to indicate some major differences.

A.1. Hydrodynamics of marine cables

The hydrodynamics of underwater cables is dominated by fluid inertia (high Reynolds number) and is effectively modeled with standard Morison drag and added mass effects [43] for a cylindrical rod in the far-field flow v_f:

$$F_{\text{drag}} = \frac{1}{2}\rho_f D\{C_n|v_r \times a_3|a_3 \times (v_r \times a_3) + \pi C_t(v_r \cdot a_3)|v_r \cdot a_3|a_3\}, \tag{23}$$

$$F_{\text{added\_mass}} = -m_a\left\{\frac{\partial v}{\partial t} + \omega \times v\right\}. \tag{24}$$

Here, $v_r = v_f - v$ is the flow relative to the rod, ρ_f is the fluid density, D is the rod diameter, C_n and C_t are the normal (form) drag and tangential (skin friction) drag coefficients, respectively, and m_a is the added mass coefficient. The rod's buoyant weight per unit length is

$$F_{\text{buoyant\_weight}} = \left(m - \rho_f \frac{\pi D^2}{4}\right) g, \tag{25}$$

where m is the rod's mass per unit length and the vector g is the acceleration due to gravity. The forces (per unit length) F_{drag}, $F_{\text{added\_mass}}$ and $F_{\text{buoyant\_weight}}$ are included in linear momentum equation (6) through the distributed force term F.

A.2. Hydrodynamics and thermal kinetics of DNA strands

The hydrodynamics of DNA is dominated by fluid viscosity (low Reynolds number) due to its small dimensions and can be effectively modeled with the distributed drag forces and moments on slender rods in Stokes flow as [13]:

$$F_{\text{drag}} = \{\xi_n a_3 \times (v_r \times a_3) + \xi_t (v_r \cdot a_3) a_3\}, \tag{26}$$

$$Q_{\text{drag}} = \{\xi_{\text{bending}} a_3 \times (\omega_r \times a_3) + \xi_{\text{torsional}} (\omega_r \cdot a_3) a_3\}, \tag{27}$$

where ξ_n and ξ_t are translational drag coefficients in the normal and tangential directions, respectively, ξ_{bending} and $\xi_{\text{torsional}}$ are rotational drag coefficients in the corresponding directions and ω_r is the fluid angular velocity relative to the rod. The drag coefficients can be determined approximately [44,45] by Oseen's model for slow flow past a cylinder [46]. DNA is nearly neutrally buoyant in its aqueous surrounding and the influence of the inertia terms in the Newton–Euler equations (6) and (7) is negligibly small.

The strain energies in DNA are often of the order of $K_b T$, where K_b is the Boltzmann constant and T is the absolute temperature of the aqueous medium. Thus, DNA mechanics are affected by the random bombardment of the surrounding fluid molecules. The thermal (or Langevin) forces exerted on DNA through these bombardments may be modeled [13] as random (white noise) external forces whose power spectrum is $4K_b T\xi_n$, where ξ_n is the (normal) drag coefficient (for proofs and more details refer to Appendix 4.3 in [13]).

Appendix 2. Constraint equations

The compatibility constraint (9) follows from the continuity (in space and time) of the transformation L from the inertial frame $\{e_i\}$ to the body fixed frame $\{a_i\}$

$$\{e_i\} = \{a_i\} L. \tag{28}$$

The ith column of L represents the directions cosines of e_i with respect to the basis $\{a_i\}$. Differentiating each unit vector e_i with respect to time (in the inertial frame) leads to

$$\left(\frac{\partial}{\partial t}\right)_{\{e_i\}} e_i = \frac{\partial L_i}{\partial t} + \omega \times L_i = 0. \tag{29}$$

Upon re-writing $\omega \times L_i = \tilde{\omega} L_i$ ($\tilde{\omega}$ is the skew-symmetric form of ω defined in Appendix 4) for all columns of L, (29) reduces to

$$\frac{\partial L}{\partial t} = -\tilde{\omega} L. \tag{30}$$

Similarly, differentiation of (28) with respect to s leads to

$$\frac{\partial L}{\partial s} = -\tilde{\kappa} L. \tag{31}$$

Since the transformation L is continuous with respect to s and t [31], we require

$$\frac{\partial}{\partial s}\left(\frac{\partial L}{\partial t}\right) = \frac{\partial}{\partial t}\left(\frac{\partial L}{\partial s}\right), \tag{32}$$

which leads to

$$\frac{\partial \tilde{\omega}}{\partial s} L - \tilde{\omega}\tilde{\kappa} L = \frac{\partial \tilde{\kappa}}{\partial t} L - \tilde{\kappa}\tilde{\omega} L \tag{33}$$

upon repeated use of (30) and (31). Post-multiplying (33) by L^{T} leads to

$$\left(\frac{\partial \tilde{\omega}}{\partial s} + \tilde{\kappa}\tilde{\omega} - \tilde{\omega}\tilde{\kappa}\right) L L^{\mathrm{T}} = \frac{\partial \tilde{\kappa}}{\partial t} L L^{\mathrm{T}}, \tag{34}$$

where we note $LL^{\mathrm{T}} = \mathrm{I}$. Noting further that $\tilde{\kappa}\tilde{\omega} - \tilde{\omega}\tilde{\kappa}$ is the skew-symmetric form of $\kappa \times \omega$ leads to the compatibility constraint

$$\frac{\partial \omega}{\partial s} + \kappa \times \omega = \frac{\partial \kappa}{\partial t}. \tag{35}$$

The inextensibility constraint (8) follows from first computing the unit tangent vector a_3. For an inextensible and unshearable Kirchhoff rod, the normal to the cross-section coincides with the tangent to the centerline, and is given by

$$\left(\frac{\partial}{\partial s}\right)_{\{e_i\}} R = a_3, \tag{36}$$

where $R(s,t)$ is the position vector. Due to continuity of $R(s,t)$ in s and t,

$$\left(\frac{\partial}{\partial t}\right)_{\{e_i\}}\left(\frac{\partial}{\partial s}\right)_{\{e_i\}} R = \left(\frac{\partial}{\partial s}\right)_{\{e_i\}}\left(\frac{\partial}{\partial t}\right)_{\{e_i\}} R = \left(\frac{\partial}{\partial s}\right)_{\{e_i\}} v = \frac{\partial v}{\partial s} + \kappa \times v. \tag{37}$$

Using (36) in (37) leads to

$$\left(\frac{\partial}{\partial t}\right)_{\{e_i\}}\left(\frac{\partial}{\partial s}\right)_{\{e_i\}} R = \left(\frac{\partial}{\partial t}\right)_{\{e_i\}} a_3 = \frac{\partial a_3}{\partial t} + \omega \times a_3 = \omega \times a_3. \tag{38}$$

Finally, equating (37) and (38) leads to the inextensibility constraint

$$\frac{\partial v}{\partial s} + \kappa \times v = \omega \times a_3. \tag{39}$$

Appendix 3. Coefficient matrices

The coefficient matrices used in (10) are provided here. Eq. (10) consolidates the field equations in the following order: (8), (9), (7) and (6). The resulting coefficient matrix K is diagonal

$$K = -\begin{bmatrix} \mathrm{I} & \Theta & \Theta & \Theta \\ \Theta & \mathrm{I} & \Theta & \Theta \\ \Theta & \Theta & B & \Theta \\ \Theta & \Theta & \Theta & \mathrm{I} \end{bmatrix} \quad \text{and} \quad M = \begin{bmatrix} \Theta & \Theta & \Theta & \Theta \\ \Theta & \Theta & I & \Theta \\ \Theta & \mathrm{I} & \Theta & \Theta \\ m\mathrm{I} & \Theta & \Theta & \Theta \end{bmatrix}. \tag{40}$$

Here, Θ is the null matrix and I is the identity matrix. The matrix $\mathbb{F}$ captures the nonlinear terms and any distributed external forces/moments

$$\mathbb{F} = \begin{Bmatrix} \omega \times a_3 - \kappa \times v \\ -\kappa \times \omega \\ -\left(\frac{\partial B}{\partial s}\kappa - \frac{\partial (B\kappa_0)}{\partial s}\right) + \omega \times I\omega + f \times a_3 - \kappa \times B(\kappa - \kappa_0) - Q \\ m(\omega \times v) - \kappa \times f - F \end{Bmatrix}. \tag{41}$$

Appendix 4. Skew-symmetric form of a vector

The cross product of two vectors x and y can be written as $x \times y = \tilde{x}y$, where

$$x = \begin{Bmatrix} x_1 \\ x_2 \\ x_3 \end{Bmatrix}, \quad y = \begin{Bmatrix} y_1 \\ y_2 \\ y_3 \end{Bmatrix} \quad \text{and} \quad \tilde{x} = \begin{bmatrix} 0 & -x_3 & x_2 \\ x_3 & 0 & -x_1 \\ -x_2 & x_1 & 0 \end{bmatrix}. \tag{42}$$

If $|x|$ is the magnitude of x and u is the unit vector along x, then the exponential of the skew-symmetric matrix $\tilde{x}$ can be expressed as

$$\exp(\tilde{x}) = \mathrm{I} + \tilde{u}\sin(|x|) + \tilde{u}^2(1 - \cos(|x|)), \tag{43}$$

where I is the identity matrix. Note that this computation employs only a scalar power series and it therefore avoids the numerical difficulties of matrix exponentiation [47].

Appendix 5. Minute random disturbance

The bifurcations that govern stability in these examples are triggered numerically upon the addition of minute random disturbances. We add these disturbances by introducing a minute random far-field flow v_f that generates drag on the rod as per Morison's formulation (23) in Appendix 1. The normal (form) drag and tangential (skin friction) drag coefficients are specified in Table 1. The random flow velocity v_f is introduced at each temporal and spatial step through a standard random number generator in the interval $[-0.5, +0.5] \times 10^{-5}$ m/s.

References

[1] F. Rosenthal, The application of Greenhill's formula to cable hockling, J. Appl. Mech. T. ASME 43 (1976) 681.
[2] C.L. Lu, N.C. Perkins, Nonlinear spatial equilibria and stability of cables under uniaxial torque, J. Appl. Mech. T. ASME 61 (1994) 879.
[3] J. Coyne, Analysis of the formation and elimination of loops in twisted cable, IEEE J. Oceanic Eng. 15 (1990) 72.
[4] E.E. Zajac, Stability of two planar loop elasticas, J. Appl. Mech. 29 (1962) 136.
[5] I. Klapper, Biological applications of the dynamics of twisted elastic rods, J. Comput. Phys. 125 (1996) 325.

[6] T. Schlick, Modeling superhelical DNA: recent analytical and dynamic approaches, Curr. Opin. Struct. Biol. 5 (1995) 245.
[7] W.K. Olson, Simulating DNA at low resolution, Curr. Opin. Struct. Biol. 6 (1996) 242.
[8] S. Goyal, N.C. Perkins, C.L. Lee, Torsional buckling and writhing dynamics of elastic cables and DNA, in: Proceedings of ASME 2003 Design Engineering and Technical Conference, Chicago, USA, September 2–6, 2003, paper no. DETC2003/MECH-48322.
[9] H. Yin, M.D. Wang, K. Svoboda, R. Landick,, S.M. Block, J. Gelles, Transcription against an applied force, Science 270 (1995) 1653.
[10] L. Finzi, J. Gelles, Measurement of lactose repressor-mediated loop formation and breakdown in single DNA molecules, Science 267 (1995) 378.
[11] R.A. Mehta, J.D. Kahn, Designed hyperstable lac repressor DNA loop topologies suggest alternative loop geometries, J. Mol. Biol. 294 (1999) 67.
[12] S.B. Smith, Y.J. Cui, C. Bustamante, Overstretching B-DNA: the elastic response of individual double-stranded and single-stranded DNA molecules, Science 271 (1996) 795.
[13] J. Howard, Mechanics of Motor Proteins and the Cytoskeleton, Sinauer Associates, Sunderland, 2001.
[14] G. KirchhoffVorlesungen Über Mathematische Physik, Mechanik, Vorl. 28, Tuebner, Leipzig, 1876.
[15] S.S. Antman, Nonlinear Problems of Elasticity, Springer, Berlin, 2004.
[16] A.E.H. Love, A Treatise on the Mathematical Theory of Elasticity, Dover Publications, New York, 1927.
[17] S.P. Timoshenko, J.M. Gere, Theory of Elastic Stability, McGraw-Hill, New York, 1961.
[18] C.L. Lu, N.C. Perkins, Complex spatial equilibria of U-joint supported cables under torque, thrust and self-weight, Int. J. Non-Linear Mech. 30 (1995) 271.
[19] I. Tobias, D. Swigon, B.D. Coleman, Elastic stability of DNA configurations. I. General theory, Phys. Rev. E 61 (2000) 747.
[20] B.D. Coleman, D. Swigon, I. Tobias, Elastic stability of DNA configurations. II. Supercoiled plasmids with self-contact, Phys. Rev. E 61 (2000) 759.
[21] G.H.M. Van der Heijden, S. Neukirch, V.G.A. Goss, J.M.T. Thompson, Instability and self-contact phenomena in the writhing of clamped rods, Int. J. Mech. Sci. 45 (2003) 161.
[22] C. Gatti-Bono, N.C. Perkins, Dynamic analysis of loop formation in cables under compression, Int. J. Offshore Polar Eng. 12 (2002) 217.
[23] C. Gatti-Bono, N.C. Perkins, Physical and numerical modelling of the dynamic behavior of a fly line, J. Sound Vibr. 225 (2002) 555.
[24] S. Goyal, N.C. Perkins, C.L. Lee, Writhing dynamics of cables with self-contact, in: Proceedings of the 5th International Symposium on Cable Dynamics, Santa Margherita Ligure, Italy, September 15–18, 2003, pp. 27–36.
[25] A. Balaeff, L. Mahadevan, K. Schulten, Structural basis for cooperative DNA binding by CAP and Lac repressor, Structure 12 (2004) 123.
[26] S. Kehrbaum, J.H. Maddocks, Effective properties of elastic rods with high intrinsic twist, in: 16th IMACS World Congress, 2000.
[27] J. Chung, G.M. Hulbert, A time integration algorithm for structural dynamics with improved numerical dissipation – The generalized-alpha method, J. Appl. Mech. T. ASME 60 (1993) 371.
[28] J.I. Gobat, M.A. Grosenbaugh, M.S. Triantafyllou, Generalized-alpha time integration solutions for hanging chain dynamics, J. Eng. Mech. ASCE 128 (2002) 677.
[29] J.I. Gobat, M.A. Grosenbaugh, Application of the generalized-alpha method to the time integration of the cable dynamics equations, Comput. Meth. Appl. Mech. Eng. 190 (2001) 4817.
[30] C.L. Bottasso, M. Borri, Integrating finite rotations, Comput. Methods Appl. Mech. Eng. 164 (1998) 307.
[31] P.E. Nikravesh, Computer-aided Analysis of Mechanical Systems, Prentice-Hall, Englewood Cliffs, NJ, 1988.
[32] D.W. Zachmann, Non-linear analysis of a twisted axially loaded elastic rod, Q. Appl. Math. 37 (1979) 67.
[33] G. Domokos, Global description of elastic bars, Z. Angew. Math. Mech. 74 (1994) T289.
[34] C.J. Benham, Onset of writhing in circular elastic polymers, Phys. Rev. A 39 (1989) 2582.
[35] M. Le Bret, Catastrophic variation of twist and writhing of circular DNAs in constraint, Biopolymers 18 (1979) 1709.
[36] T.J. Healey, Material symmetry and chirality in nonlinearly elastic rods, Math. Mech. Solids 7 (2002) 405.
[37] G.A. Costello, Theory of Wire Rope, Springer, New York, 1997.
[38] J.F. Marko, Stretching must twist DNA, Europhys. Lett. 38 (1997) 183.
[39] C. Branden, J. Tooze, Introduction to Protein Structure, Garland Publishing, New York, 1999.
[40] C.R. Calladine, H.R. Drew, B.F. Luisi, A.A. Travers, Understanding DNA, the Molecule and How It Works, Academic Press, London, 2004.
[41] A.L. Lehninger, D.L. Nelson, M.M. Cox, Lehninger Principles of Biochemistry, Worth Publishers, 2005.
[42] M. Lewis, G. Chang, N.C. Horton, M.A. Kercher, H.C. Pace, M.A. Schumacher, R.G. Brennan, P.Z. Lu, Crystal structure of the lactose operon repressor and its complexes with DNA and inducer, Science 271 (1996) 1247.
[43] J.R. Morison, M.P. O'Brien, J.W. Johnson, S.A. Schaaf, The force exerted by surface waves on piles, T. Am. I. Min. Mat. Eng. 189 (1950) 149.

[44] M.M. Tirado, J. Garciadelatorre, Translational friction coefficients of rigid symmetric top macromolecules – Application to circular-cylinders, J. Chem. Phys. 71 (1979) 2581.
[45] M.M. Tirado, J. Garciadelatorre, Rotational-dynamics of rigid symmetric top macromolecules – Application to circular-cylinders, J. Chem. Phys. 73 (1980) 1986.
[46] H. Lamb, Hydrodynamics, Dover Publications, New York, 1945.
[47] C. Moler, C. Van-Loan, 19 Dubious ways to compute exponential of a matrix, SIAM Rev. 20 (1978) 801.